Electronic Supplementary Material (ESI) for Soft Matter.


## Supplementary Figures

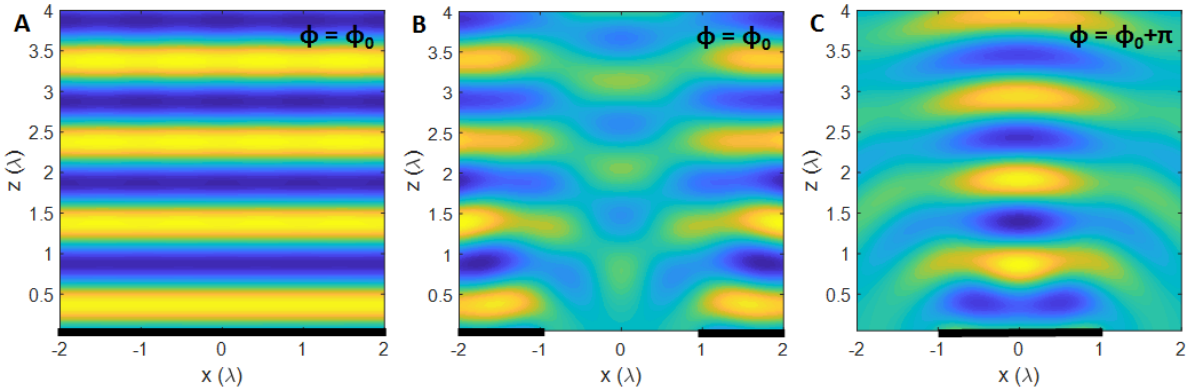


**Figure S1:** Properties of finite transducers. All three cases (A,B and C) are modelled separately according to the Huygens-Fresnel principle, where the pressure magnitude in the fluid at a given point is equal to the sum of the contributions from all points along the transducer extent. Case A shows a series of planar wavefronts arising from a transducer whose extent is much larger than the shown region ($W = 100\lambda$). The transducer extent in case B is identical, with the exception of a non-emitting region between $-\lambda < x < \lambda$. Case C can be deduced in one of two ways: either as an independent wavefield with a 180° phase difference (with $\varphi_C = \varphi_{A,B} + \pi$) from case A and B, or by subtracting case B from case A ($C = A - B$). Equivalently, the wave field in case B can be derived by adding the wavefield from case C to A ($B = A + C$). Accordingly, the effect of a finite transducer extent can be modelled by adding an oppositely-phased wavefront from where the transducer isn't.

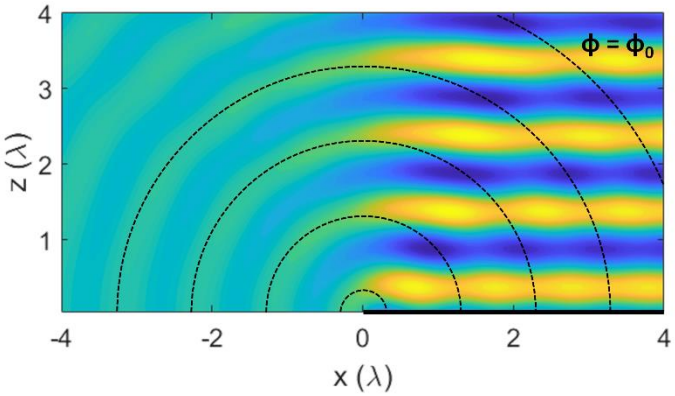


**Figure S2**: The effect of edge waves, or rather that of a spatially limited transducer extent, on the wavefronts emanating from a transducer (black line from $x = 0$ to $x = 4\lambda$) can be seen in this plot of the transient pressure field. The expanding cylindrical waves (dotted black lines) from the transducer edge interfere with the planar wavefronts that ultimately results in regions of high-and low time-averaged pressure.

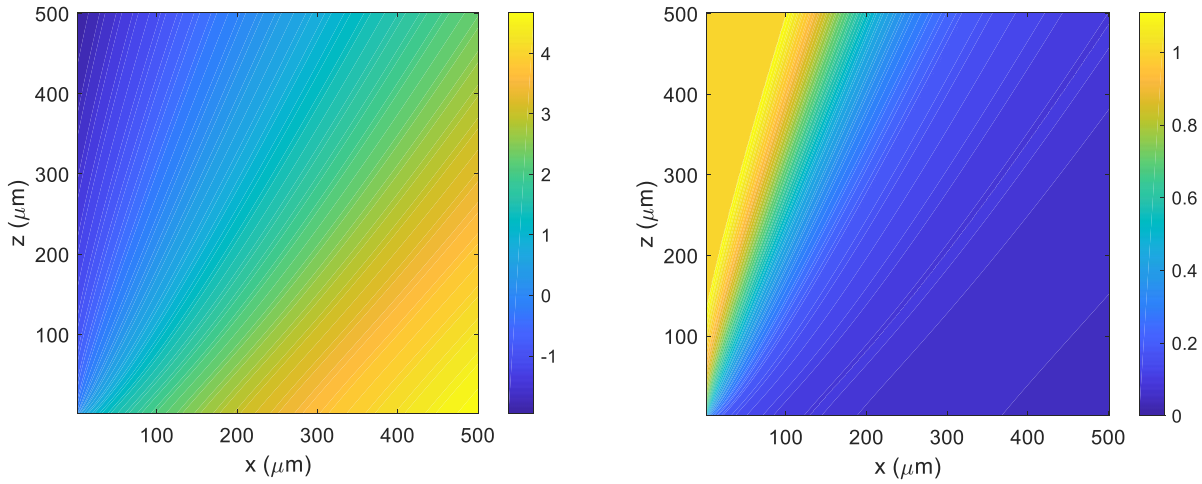


**Figure S3**: Plot of the Fresnel-Kirchoff parameter υ (left) and diffraction coefficient $D(\theta_h, r)$ (right). At the rightmost extent of this figure near $z = 0$ (at $x = 500$ µm with a 100 µm SAW wavelength), the value of $D(\theta_h, r) \approx 5\%$ of the acoustic beam maximum. The beam projects up from the lower left at $\theta_R$.

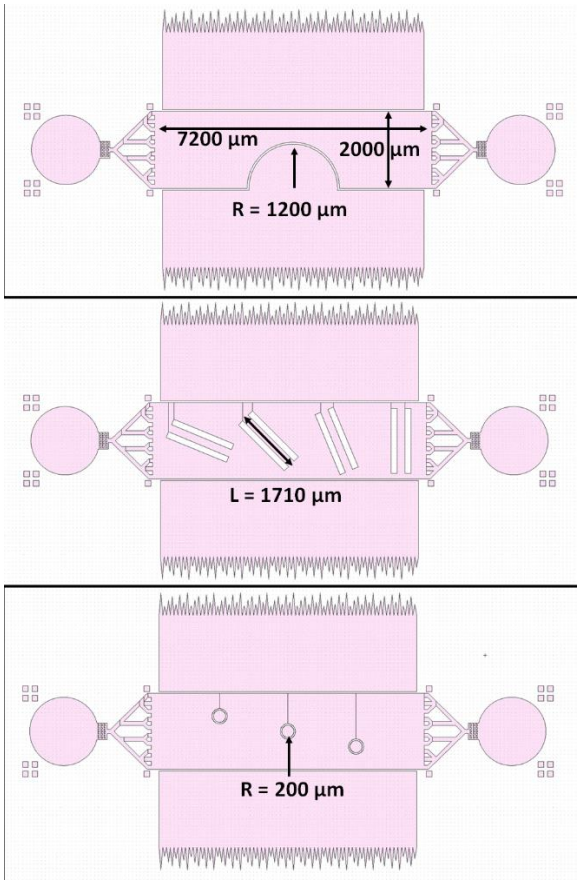


**Figure S4**: Channel designs and relevant distances used in (from top to bottom) Figures 1, 6 and 7. IDTs are aligned in the air pocket regions on top or below the the channel in the center.

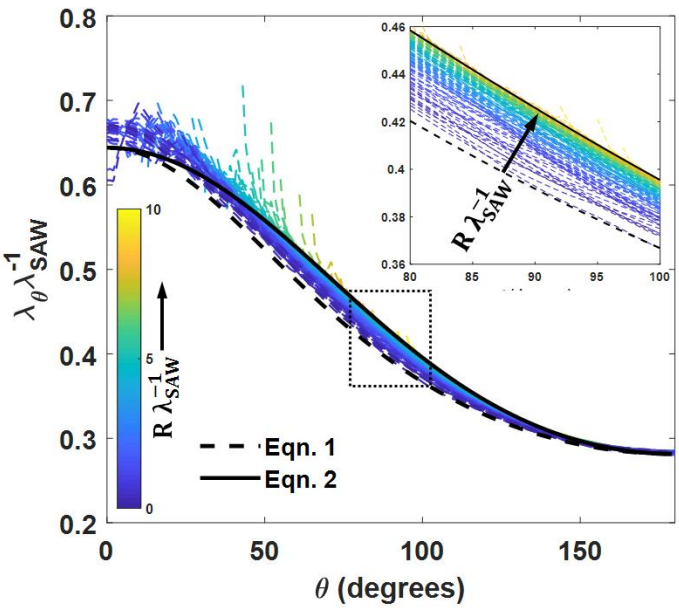


**Figure S5:** Simulated values of $\lambda_\theta$ relative to $\lambda_{\mathrm{SAW}}$ according to the model presented in Figure 6. This figure here shows the transition between predictions made by Equation 1 and Equation 2 for $R\lambda_{\mathrm{SAW}}^{-1} = 0.1$ to $R\lambda_{\mathrm{SAW}}^{-1} = 10$ and $\tilde{c} = 0.4$, though predictions are relatively non-uniform relative to those arising from the quasi-analytical method (shown in Figure S4), especially for smaller values of $\theta$; this is due to the influence of interference lobes that can be observed in the Figure 6 simulations.

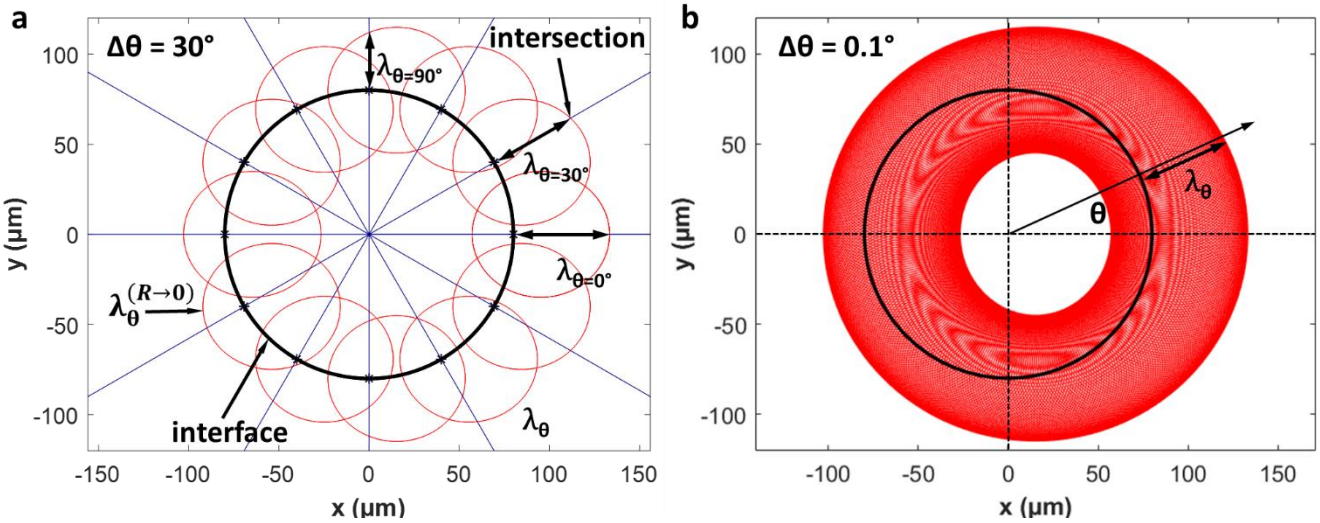


**Figure S6:** Increase in periodic spacing above that predicted by Equation 1 for finite-sized objects. (a) This figure demonstrates that the evolved time-averaged field around an object (black circle) can be composed of the sum of intersection ellipsoids (as in Figure 2a) from every point on the object surface according the Huygens-Fresnel principle. Red lines show the ellipsoids for a select number of points. The value of $\lambda_\theta$ is given by distance between the object surface and the outermost intersection of a radial line with any intersection ellipsoid. To clearly show the methodology intersection ellipsoids are plotted every 30°. (b) The accurate determination of $\lambda_\theta$ is enhanced for decreasing $\Delta\theta$ between plotted ellipses, here with $\Delta\theta$ = 0.1°.